INTERNATIONAL JOURNAL OF HYDROGEN ENERGY XXX (2016) 1–13

Available online at www.sciencedirect.com

ScienceDirect

journal homepage: www.elsevier.com/locate/he

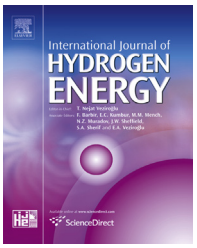

A comparison of evaporative and liquid cooling methods for fuel cell vehicles

A. Fly[*], *R.H. Thring*

Dept. Aeronautical and Automotive Engineering, Loughborough University, Loughborough, Leicestershire, UK

ARTICLE INFO

Article history:
Received 24 March 2016
Received in revised form
26 May 2016
Accepted 7 June 2016
Available online xxx

Keywords:
Thermal management
Water balance
Fuel cell vehicle
PEM
Heat transfer
Cooling

ABSTRACT

Despite having efficiencies higher than internal combustion engines, heat rejection from fuel cells remains challenging due to lower operating temperatures and reduced exhaust heat flow. This work details a full system simulation which is then used to compare a conventional liquid cooled fuel cell system to two types of evaporatively cooled fuel cell systems. Both steady state and transient operation are considered. Results show the radiator frontal area required to achieve thermal and water balance for an evaporatively cooled system with an aluminium condensing radiator is 27% less than a conventional liquid cooled system at 1.25 A/cm^2 steady state operation. The primary reason for the reduction is higher heat transfer coefficients in the condensing radiator due to phase change. It is also shown that the liquid water separation efficiency has a significant influence on the required radiator frontal area of the evaporatively cooled system.

Introduction

Hydrogen fuel cells are an alternative power source to the internal combustion engine for vehicle applications due to zero harmful exhaust emissions, high efficiencies and the potential to generate hydrogen from renewable methods. There are many issues to be addressed before the widespread uptake of hydrogen fuel cell vehicles, one such issue is how to effectively remove waste heat from the electrochemical reaction of PEM (Proton exchange membrane) fuel cells. The low exhaust heat flow of PEM fuel cells compared to the internal combustion engine (IC) means that, despite higher efficiencies, the heat rejected to the cooling system is higher in fuel cell vehicles [1]. This combined with lower operating temperatures, limited by the boiling point of water, creates a significant demand on the vehicle thermal management system. Previous studies which have compared the heat exchanger requirements of internal combustion and fuel cell powertrains have concluded that fuel cell vehicles require radiator frontal areas two to four times the size of conventional internal combustion engines of equal power and up to four times the cooling air flow [1–3].

Fuel cell cooling

Fuel cell cooling can generally be split into three categories, air cooling, liquid cooling and cooling through phase change; a detailed review of these different methods is presented by Zhang and Kandlikar [4].

Air cooling

Passing ambient air either through the cathode or through additional cooling plates between cells is the simplest method

* *Corresponding author.*
E-mail address: A.Fly@Lboro.ac.uk (A. Fly).

http://dx.doi.org/10.1016/j.ijhydene.2016.06.089

of removing waste heat from fuel cells since minimal balance of plant is required. Several examples of air cooled fuel cell vehicles exist in the literature, the Microcab H2EV utilises a 3.0 kW Horizon open cathode fuel cell in a battery hybrid arrangement [5] and the Suzuki Burgmann fuel cell scooter which utilises a 1.6 kW air cooled stack [6]. Air cooled fuel cells are most commonly used in applications, such as in the two examples, where the rated power is less than 5 kW [7]. As electrical power (and hence required heat removal) increases, cooling air flow and heat transfer area required passes the point where it becomes more beneficial to have either a liquid or phase change cooling loop and a separate radiator optimised for heat transfer. Odabaee et al and Boyd and Hooman [8,9] investigated improving heat transfer through using metal foams, showing improved performance at the expense of high pumping losses. More recently Afshari et al [10], conducted a numerical study on liquid flow through metal foams as coolant flowfields, showing both reduced temperature variation and lower pressure loss compared to conventional serpentine.

Liquid cooling

Convective heat transfer to liquid coolant is the most commonplace method of removing waste heat from higher power PEM fuel cell stacks (>5 kW) [7]. Waste heat is transferred from the cell, through the bi-polar plate and into the coolant which flows through separate cooling channels between selected cells. Heated coolant is then pumped to a separate heat exchanger where it is either rejected to ambient or used for alternative purposes such as heating. The comparison of different cooling channel geometries and flowfield designs through numerical simulations has received significant attention in the literature, including [11–14] among others. Chen et al and Baek et al [11,12] looked at the temperature distribution and pressure drop for different flowfield designs, Sasmito et al and Kang et al [13,14] also demonstrated how different configurations influenced the overall net power output of the fuel cell. To avoid significant thermal gradients across the cell, the change in liquid coolant temperature from inlet to outlet should be kept small [15,16]. Stack temperature is regulated by varying the inlet coolant temperature and coolant flow rate, requiring the thermal management system to closely match fuel cell stack power demand.

Previous studies have shown good ability to regulate stack temperature within acceptable limits using conventional control methods. Cheng et al [17] varied radiator fan speed on a fuel cell bus using feedforward/feedback optimal control to regulate stack temperature. Yu and Jung [16] and Saygili et al [18] controlled stack temperature by simultaneously varying coolant flow rate and radiator fan speed. Yu and Jung [19] used PWM (pulse width modulation) and PI (proportional integral) control to regulate stack temperature by varying the radiator fan speed, target stack coolant inlet temperature was obtained through varying the coolant flow rate, the target inlet temperature was based on their previous modelling study [16]. Saygili et al [18] created a semi-empirical PEM fuel cell model based on a 3 kW system to compare PWM and PI control of the radiator fan, the authors also investigated three different control methods for the coolant flow rate pump; fixed voltage, compressor tracking (feedforward) and PI (feedback). Alternatively Hu et al. and Ahn and Choe [20,21] regulated stack temperature by controlling the amount of coolant which bypasses the radiator. Hu et al [20] controlled the by-pass opening factor to achieve a desired stack temperature, comparing conventional PI and fuzzy logic based feedback control, whereas Ahn and Choe [21] compared PI and state feedback control. All of the above studies have managed to regulate stack temperature to within ±2 °C across transient current profiles. An advantage of liquid cooled systems are that they can utilise existing vehicle radiators and cooling system architecture. However, lower operating temperatures compared to IC engines require larger radiator frontal areas to achieve thermal balance. Fronk et al and Rogg et al [1,3] have both looked at novel radiator designs to try to minimise radiator sizes in fuel cell vehicles. Islam et al and Zakaria et al [22,23] investigated the potential of using nanofluids in the liquid coolant loop of PEM fuel cell stacks, Islam et al [22] claimed up to a 10% reduction in radiator frontal area from using a nanofluid compared to conventional water/ethylene glycol coolant mix.

Phase change cooling

Phase change cooling utilises the enthalpy of vapourisation to remove waste heat from the fuel cell and can be further separated into heat pipes, flow boiling and evaporative cooling. Whilst heat pipes have been shown to be effective for passive heat removal from small fuel cell stacks [24], the required condenser areas and short pipe lengths make current designs better suited to heat spreading in low power applications. Flow boiling with application to PEM fuel cells has been experimentally studied by Garrity et al and Soupremanien et al [25,26]. Both works represented fuel cell irreversibilities using a heat pad, demonstrating the potential for reduced pumping load, good temperature uniformity and specific heat rejection up to three times higher than liquid cooling [26]. Flow boiling has further potential to improve fuel cell vehicle cooling as the high heat transfer coefficients seen in the condenser may help to reduce heat exchange areas required. However, this technology has yet to be developed at a stack level scalable to automotive sized powertrains.

Evaporative cooling through introducing liquid water into the flow channels of the fuel cell has been studied by several authors. This method of cooling has the additional benefit of internally humidifying the cell, removing the need for both external humidifiers and separate cooling plates within the stack; although a condenser is required to reclaim the evaporated water. Evaporatively cooled stacks have been experimentally demonstrated by Refs. [27–30]. Meyers et al [27] used capillary action to introduce liquid water into the cathode flow channels through a porous plate, demonstrating results in a 30 cell stack. Wood et al [28] injected liquid water into the anode inlet stream combined with interdigitated flow channels within the cell to achieve evaporative cooling. Hwang and Kim [30] used a water atomiser in the cathode inlet for humidification, providing up to 10% of the fuel cell stack heat removal through evaporation and Warburton et al [29] demonstrated a 30kWe evaporatively cooled system in an automotive application with cold start ability. Modelling of evaporatively cooled fuel cell stacks has been studied by Refs. [31–34]. Schultze and Horn [31] produced a stack model for control based studies, Refs. [32–34] used simulations to study

Please cite this article in press as: Fly A, Thring RH, A comparison of evaporative and liquid cooling methods for fuel cell vehicles, International Journal of Hydrogen Energy (2016), http://dx.doi.org/10.1016/j.ijhydene.2016.06.089

the temperature regulation and liquid water requirements of evaporatively cooled fuel cell stacks.

This paper seeks to compare the two most currently viable cooling methods for fuel cell vehicles with a high power stack, which have been identified as liquid cooling and evaporative cooling. Comparisons are conducted through the use of system level simulations, with the aim to quantitatively compare the heat exchanger requirements for the different systems and alternative system layouts including both steady state and thermal transients.

Fuel cell system

The models used for comparison are based on a 60 kW, 360 cell PEM fuel cell system. The fuel cell model remains identical for both cooling methods with the exception of an additional term for liquid water addition in the evaporatively cooled stack and for heat transfer to coolant in the liquid cooled system. Details of the fuel cell model are presented in the modelling section.

Liquid cooled (LC) system

The liquid cooled system considered in this study is shown in Fig. 1a. Heat is removed from the stack via forced convection of liquid water through circular channels within the bi-polar plates. A conventional liquid to air cross flow louvred fin radiator is used to reject waste heat to the environment. Stack temperature is regulated via feedback control of the radiator by-pass valve, temperature increase of the coolant across the stack is maintained at a maximum of 5 °C using a variable flow rate pump. The inlet cathode gas is humidified using a vapour exchange system from the cathode exhaust, the anode is dead ended.

Evaporatively cooled (EC) system

Two different evaporatively cooled thermal management systems are included in this study, in both cases the fuel cell stack is the same. Liquid water is added into the cathode flow channels, here it evaporates, and in the process both humidifies the cells and removes the waste heat. The cathode exhaust is then cooled, condensing the evaporated water along with some of the product water, the condensed water is then separated in a cyclone and stored in a water tank for future use. The simplest of the two systems uses a louvred fin radiator to remove heat from the cathode exhaust, this layout is shown in Fig. 1b and in this paper is referred to as Layout B. One problem with the condensing radiator layout is that the water added into the cell must remain de-ionised, and as such mass manufactured aluminium radiators should be avoided to reduce cell degradation rates [35]. An alternative is to use an intermediate condenser to transfer heat to a water/glycol cooling loop and use a conventional aluminium radiator. This system is illustrated in Fig. 1c and in this paper is referred to as the Layout C. One advantage of the intermediate condenser system is that the coolant loop can be combined with the vehicle ancillary cooling loads to reduce the number of heat exchangers compared to the condensing radiator.

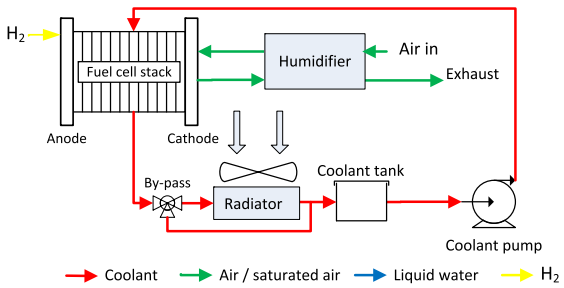

(a) Layout A: Liquid cooled

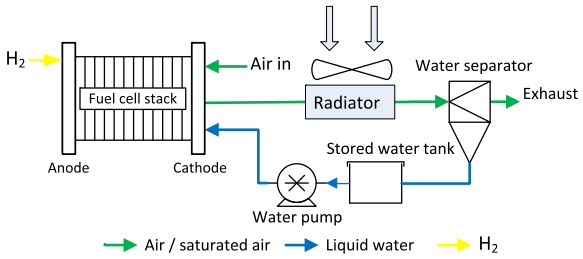

(b) Layout B: Evaporatively cooled with condensing radiator

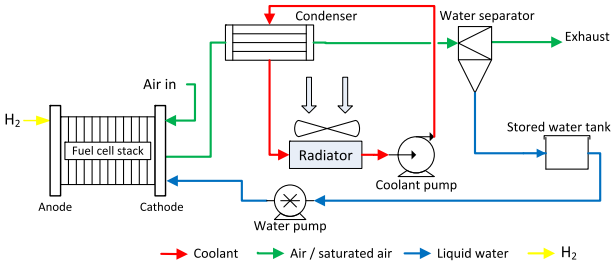

(c) Layout C: Evaporatively cooled with intermediate cooling loop

Fig. 1 – Fuel cell system layouts.

Modelling

Fuel cell stack model

The fuel cell stack is modelled as a lumped parameter system with interacting sub-models for the anode and cathode mass balance, cell voltage, energy balance and membrane hydration. The same model is used for both the liquid cooled and evaporatively cooled systems, the only differences being the inclusion of a water injection term $\dot{m}_{H_2O,inject}$ in the mass conservation section for the evaporatively cooled system and the inclusion of $\dot{Q}_{coolant}$ in the energy balance section for the liquid cooled model. The model makes the following assumptions:

- All gases are ideal.
- Spacial variation across the cell is not considered.
- Liquid water is assumed to evaporate up to saturation.
- Flooding effects are ignored.
- Diffusion of inert gases across the membrane are not considered.

Cell voltage

Cell voltage is determined from the open circuit voltage and significant irreversibilities as a function of the current density.

Please cite this article in press as: Fly A, Thring RH, A comparison of evaporative and liquid cooling methods for fuel cell vehicles, International Journal of Hydrogen Energy (2016), http://dx.doi.org/10.1016/j.ijhydene.2016.06.089

Open circuit voltage (E_n) is determined using Equation (1) [7], activation overvoltage (V_{act}) and diffusion of hydrogen from anode to cathode (fuel crossover (V_{fc})) are modelled using the Tafel equation, where exchange current density (i_{oc}) is corrected for changes in pressure and temperature using Equation (3) [15]. Mass transport losses (V_{trans}) at increased current densities are modelled using the empirical exponential relationship of Equation (4) [7], voltage loss due to membrane resistance is simulated using Ohm's law (Equation (5) (V_{ohm})). Finally cell voltage (V_{cell}) is the sum of the open circuit voltage and overvoltages, stack voltage is the product of cell voltage and number of cells, assuming uniform performance across all cells.

$$E_n = -\frac{\Delta\hat{h} - T\Delta\hat{s}}{2F} + \frac{RT}{2F} ln\left(\frac{P_{H_2} P_{O_2}^{\frac{1}{2}}}{1}\right) \tag{1}$$

$$V_{act} + V_{fc} = \frac{RT}{2\alpha F} ln\left(\frac{i + i_n}{i_{oc}}\right) \tag{2}$$

$$i_{oc} = i_{oc,0}\left(\frac{P_{H_2}}{P_0}\right)^{\gamma} exp\left[-\frac{E_c}{RT_s}\left(1 - \left(\frac{T_s}{T_0}\right)\right)\right] \tag{3}$$

$$V_{trans} = a_{trans} exp(b_{trans} i) \tag{4}$$

$$V_{ohm} = \Omega i \tag{5}$$

$$V_{cell} = E_n - V_{act} - V_{fc} - V_{trans} - V_{ohm} \tag{6}$$

Membrane model

Membrane water content (H_2O molecules per $SO_3^-H^+$ site) is found as a function of vapour activity (a_m) in both the cathode and anode using Equation (7) [36]. Mean membrane water content is then used to determine the electro-osmotic drag coefficient (n_{drag}) and protonic conductivity (σ) [36]. Membrane resistance (Ω) is obtained assuming a uniform conductivity across the thickness of the membrane. Water vapour diffusivity is determined using the piecewise approximation of [37], with the third line adapted by Chen and Peng [38] to prevent a discontinuity at $\lambda = 4.5$. Equation (13) is then used to find the net water flow across the membrane as the sum of both electro-osmotic drag and back diffusion where A is the stack active area in cm^2.

$$\lambda = \begin{cases} 0.043 + 17.81a_m - 39.85a_m^2 + 36.0a_m^3 & a_m < 1 \\ 14 + 1.4(a_m - 1) & a_m > 1 \end{cases} \tag{7}$$

$$n_{drag} = \frac{2.5\lambda}{22} \tag{8}$$

$$D_\lambda = exp\left(2416\left(\frac{1}{303} - \frac{1}{T_s}\right)\right) D_{\lambda,30} \tag{9}$$

$$D_{\lambda,30} = \begin{cases} 1 \times 10^{-6} & \lambda < 2 \\ (1 + 2(\lambda - 2))10^{-6} & 2 \le \lambda \le 3 \\ (3 - 1.167(\lambda - 3))10^{-6} & 3 < \lambda \le 4.5 \\ 1.25 \times 10^{-6} & \lambda \ge 4.5 \end{cases} \tag{10}$$

$$\sigma = exp\left(1268\left(\frac{1}{303} - \frac{1}{T_s}\right)\right)\sigma_{30} \tag{11}$$

$$\sigma_{30} = 0.005139\lambda - 0.00326 \quad \lambda > 1 \tag{12}$$

$$\dot{m}_{H_2Otrans} = M_{H_2O} A\left(\frac{n_{drag} i}{F} - \frac{\rho_{dry}}{M_{mem}} D_\lambda \frac{d\lambda}{dz}\right) \tag{13}$$

Mass conservation

Mass balance is determined separately for each species in each volume. Four volumes are considered in the model; anode, cathode, cathode inlet and cathode outlet manifolds. Equations (14)–(16) show mass balance equations for the cathode. In the evaporatively cooled model $\dot{m}_{H_2Oinject}$ represents the amount of water added to achieve a desired humidity within the cathode flow channel, this is calculated using a PI (proportional integral) controller to achieve a 100% target relative humidity. In the liquid cooled model the $\dot{m}_{H_2Oinject}$ term is always zero. Equations (17) and (18) show mass balance equations for the anode volume. $\dot{m}_{O_2reac}$ and $\dot{m}_{H_2reac}$ are the mass fluxes of oxygen and hydrogen consumed by the electrochemical reaction respectively, $\dot{m}_{H_2Oreac}$ is the mass flux of liquid water produced, $\dot{m}_{H_2Otrans}$ is the net mass flow rate of water transferred from anode to cathode across the membrane. Flow rates into the system are determined from the requested reactant stoichiometries, gas exit flow from each lumped volume is found using the linearised nozzle equation [39] (Equation (19)). System back pressure is regulated through changing the cross sectional area of the exit manifold nozzle (A_n) using a PI controller, system pressures refer to fuel cell exit pressure, pre condenser. All liquid water is assumed to evaporate up until the point where the volume reaches saturation, excess water will remain in liquid form. Liquid water can be removed from the flow channels in one of two ways, either through evaporation once the saturation limits change or as droplets of liquid water entrained in the gas flow. The later is simulated as an empirical function of gas mass flow rate and accumulated liquid water mass, a value of two has been arbitrarily chosen for constant (τ) [31]. Fuel and water lost from a dead-ended anode with periodic purging are represented using a constant anode stoichiometry of 1.03, Rabbani and Rokni [40] indicated that this level of anode bleed is sufficient to prevent the build up of Nitrogen and water in the anode.

$$\frac{dm_{O_2,ca}}{dt} = \dot{m}_{O_2in} - \dot{m}_{O_2out} - \dot{m}_{O_2reac} \tag{14}$$

$$\frac{dm_{N_2,ca}}{dt} = \dot{m}_{N_2in} - \dot{m}_{N_2out} \tag{15}$$

$$\frac{dm_{H_2O,ca}}{dt} = \dot{m}_{H_2Oin} + \dot{m}_{H_2Oinject} + \dot{m}_{H_2Oreac} - \dot{m}_{H_2Oout} + \dot{m}_{H_2Otrans} \tag{16}$$

$$\frac{dm_{H_2,an}}{dt} = \dot{m}_{H_2in} - \dot{m}_{H_2out} - \dot{m}_{H_2reac} \tag{17}$$

$$\frac{dm_{H_2O,an}}{dt} = \dot{m}_{H_2Oin} - \dot{m}_{H_2Oout} - \dot{m}_{H_2Otrans} \tag{18}$$

$$\dot{m}_{out} = C_n A_n (P_1 - P_2) \tag{19}$$

Please cite this article in press as: Fly A, Thring RH, A comparison of evaporative and liquid cooling methods for fuel cell vehicles, International Journal of Hydrogen Energy (2016), http://dx.doi.org/10.1016/j.ijhydene.2016.06.089

$$\dot{m}_{H_2O,l} = \tau \dot{m}_{gas} m_{H_2O,l} \quad (20)$$

Energy balance

Energy balance is determined at a stack level assuming a uniform stack temperature using Equation (21). $\dot{Q}_{reac}$ is the energy liberated from the higher heating value (HHV) of the hydrogen reacted and $\dot{Q}_{elec}$ the electrical energy produced by the stack. $\dot{Q}_{in}$ and $\dot{Q}_{out}$ represent the sum of enthalpy into and out of the stack using Equation (22), where j represents each species. In the liquid cooled model $\dot{Q}_{coolant}$ represents the thermal energy transfer from the fuel cell stack to the liquid coolant through the flow channels and is discussed in the liquid cooling section, for evaporative cooling $\dot{Q}_{coolant}$ is always zero.

$$m_s C_{p,s} \frac{dT_s}{dt} = \dot{Q}_{reac} + \dot{Q}_{in} - \dot{Q}_{elec} - \dot{Q}_{out} - \dot{Q}_{coolant} \quad (21)$$

$$\dot{Q} = \dot{m}_v \Delta H_v + \sum_{j=1}^{n} \dot{m}_j C_{pj} (T - T_0) \quad (22)$$

Fuel cell stack validation

The fuel cell stack model has been validated using cell voltage data from a 30 cell evaporatively cooled stack with a cell active area of 320 cm^2 [27]. Fig. 2 compares the experimental and simulated cell voltage for a 1.67 cathode stoichiometry, 80% cathode humidity. Further validation was conducted by an industrial partner using a 15 kW stack to compare predicted and experimental cell temperatures for evaporative cooling. Across a range of operating conditions, including different current densities and cathode stoichiometries, a 1.5 °C mean absolute temperature error was observed.

Single phase radiator

The single phase radiator is used in the liquid cooled system (layout A) and the evaporatively cooled system featuring the intermediate cooling loop (layout C). Modelled as a cross flow tube and fin aluminium heat exchanger, the hot side is a liquid water/glycol mixture and the cold side ambient air flow. The effectiveness number of transfer units method (ε-NTU) is used to determine the overall heat transfer. Assuming a uniform air flow over the radiator and even distribution of coolant into each tube, heat transfer can be modelled for a single cooling tube then multiplied by the number of tubes within the radiator core. The Dittus–Boelter correlation [41] is used to determine the hot side Nusselt number, cold side heat transfer coefficient is determined using Equation (23) where j is the Colburn factor, found as an empirical function of louvred fin geometry [42], the radiator geometry used in this study is shown in Table 2. Once both heat transfer coefficients are known the overall heat transfer coefficient (Equation (24)) can be found, along with the heat capacity ratio (Equation (25)) and number of transfer units (Equation (26)). The effectiveness and finally heat transfer can be determined using Equations (27) and (28) respectively where n_{tubes} is the total number of cooling tubes in the radiator.

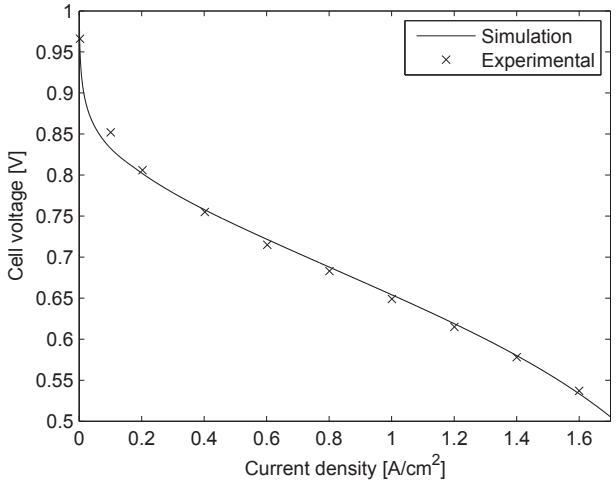

Fig. 2 – Cell voltage validation, experimental data from Ref. [27].

$$h_{air} = \frac{j \dot{m}_{air,fin} C_{p,air}}{A_{fin} Pr_{air}^{\frac{2}{3}}} \quad (23)$$

$$UA = \left[\frac{1}{h_h \pi d_h L} + \frac{\ln\left(\frac{d_h + 2t_w}{d_h}\right)}{2\pi k_w L} + \frac{1}{\eta_c h_c A_c} \right]^{-1} \quad (24)$$

$$C_r = \frac{C_{min}}{C_{max}} \quad (25)$$

$$NTU = \frac{UA}{C_{min}} \quad (26)$$

$$\varepsilon = 1 - exp\left[\left(\frac{1}{C_r}\right) NTU^{0.22} \left(exp\left(-C_r NTU^{0.78}\right) - 1\right) \right] \quad (27)$$

$$\dot{Q}_{rad} = \varepsilon n_{tubes} C_{min} \left(T_{h,in} - T_{c,in}\right) \quad (28)$$

Radiator geometry based on Ref. [43] (Table 2) has been used with changes in the core width and height to change frontal area. Comparison of the predicted heat transfer to those measured in Ref. [43] can be seen in Fig. 3 showing a good agreement in heat transfer across a variety of air and coolant flow rates with a 4.2% mean absolute error.

Condenser models

Two separate condensers are considered in this study, a condensing radiator used in layout B and a compact plate condenser used in layout C. The hot side of both condensers is the cathode exhaust, a mixture of condensable water vapour and non-condensable Oxygen and Nitrogen. In the condensing radiator the cathode exhaust mixture flows downward inside vertical tubes in a cross flow fin and tube heat exchanger, the cold side being ambient air flow. In the compact plate condenser the cathode exhaust mixture flows between multiple pressed plates with chevron flow patterns, the cold side is the liquid coolant loop running in counterflow through alternating plates.

The hot side calculations of both condensers are based on an adapted version of the iterative model developed by No and

Please cite this article in press as: Fly A, Thring RH, A comparison of evaporative and liquid cooling methods for fuel cell vehicles, International Journal of Hydrogen Energy (2016), http://dx.doi.org/10.1016/j.ijhydene.2016.06.089

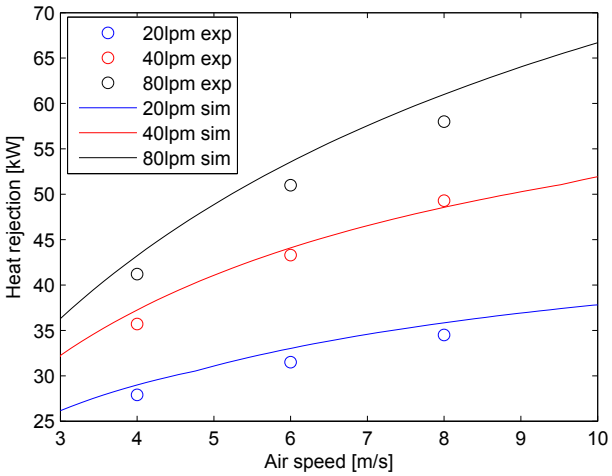

Fig. 3 – Radiator validation, experimental data from Ref. [43].

Park [44]. The original model has been modified to account for conditions seen in a fuel cell exhaust, including variation in oxygen content, superheating and pressure drop. As vapour condenses from the free stream onto the wall surface, a condensate boundary layer is formed, this leaves behind a second boundary layer of gas with a lower mass fraction of condensable water vapour and higher mass fraction of non-condensable gas. Once established, water vapour must first transfer across the non-condensable boundary before condensing at the liquid water interface. The mass transfer resistance of water vapour across the non-condensable gas boundary severely impedes heat transfer compared to pure condensation and needs to be accounted for [45]. Fig. 4 illustrates the double boundary layer and partial pressure profiles within the non-condensable layer. The variation in non-condensable mass fraction along the heat exchanger length due to condensation can cause the hot side heat transfer coefficient to vary by an order of magnitude between inlet and outlet [46]. To account for such changes a one-dimensional model has been used in this work. In this case the heat transfer area of both models is separated into 100 sections. Since the calculation of heat transfer coefficient requires prior knowledge of the temperature at the interface between the condensate layer and non-condensable boundary layer, an iterative calculation method has been used.

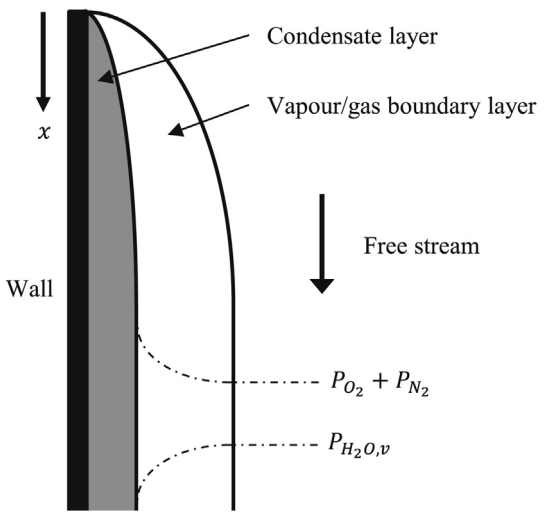

Fig. 4 – Illustration of double boundary layer method.

Hot side heat transfer

The heat flux of the radiator hot side (Equation (29)) is calculated using the total hot side heat transfer coefficient (h_t) and temperature difference between the bulk gas and hot side wall. h_t represents a parallel combination of the sensible and condensation heat transfer coefficients between the bulk gas and film surface in series with the thermal resistance across the condensate layer to the wall, shown in Equation (30).

$$q_t = h_t(T_b - T_{wall,h}) \tag{29}$$

$$\frac{1}{h_t} = \frac{\delta}{k} + \frac{1}{h_{cd} + h_{cv}} \tag{30}$$

The heat transfer coefficient due to condensation (h_{cd}) is equal to the product of the enthalpy of vapourisation of liquid water and the water vapour flux from the bulk to the condensate layer (condensation rate). The condensation rate is determined from the gradient of water vapour concentration between the bulk and the interface and the mass transfer coefficient, shown in Equation (31).

$$h_{cd} = g\Delta H_v \frac{W_{v,i} - W_{v,b}}{(1 - W_{v,i})(T_i - T_b)} \tag{31}$$

Water vapour mass fraction in the bulk flow mixture ($W_{v,b}$) can be determined from the known mass flow rate of each species using Equation (32). Interface water vapour mass fraction (W_{vi}) can be calculated assuming saturation at an estimated interface temperature, the estimate is later refined in the iterative procedure.

$$W_{v,b} = \frac{\dot{m}_{v,b}}{\dot{m}_{v,b} + \dot{m}_{N_2,b} + \dot{m}_{O_2,b}} \tag{32}$$

The Stanton number (St) is used to determine both the heat transfer coefficient (Equation (33)) and mass transfer coefficient (Equation (34)) by applying the heat and mass transfer coefficient analogy and using the Dipprey correlation for rough tubes. Equation (35) is used to determine the relative roughness inside the pipe from the interfacial friction factor. The Wallis correlation (Equation (36)) is used to calculate the friction factor at the condensate/gas interface assuming vertical annular flow. The Petukhov correlation is used to find the friction factor in a smooth pipe (f) used in Equation (36) [44].

$$St_{ht} = \frac{\frac{f_i}{2}}{1 + \sqrt{\frac{f_i}{2}}\left(5.19\left(Re_b\sqrt{\frac{f_i}{2}}\,\frac{\omega}{d_h}\right)^{0.2} Pr_b^{0.44} - 8.48\right)} = \frac{Nu}{Re_b Pr_b} \tag{33}$$

$$St_{mt} = \frac{\frac{f_i}{2}}{1 + \sqrt{\frac{f_i}{2}}\left(5.19\left(Re_b\sqrt{\frac{f_i}{2}}\,\frac{\omega}{d_h}\right)^{0.2} Sc_b^{0.44} - 8.48\right)} = \frac{g}{\rho_b V_b} \tag{34}$$

Please cite this article in press as: Fly A, Thring RH, A comparison of evaporative and liquid cooling methods for fuel cell vehicles, International Journal of Hydrogen Energy (2016), http://dx.doi.org/10.1016/j.ijhydene.2016.06.089

$$\frac{\omega}{d_h} = exp\left(3 - 0.4\left(\frac{f_i}{2}\right)^{-0.5}\right) \tag{35}$$

$$f_i = f\left(1 + 300\frac{\delta}{d_h}\right) \tag{36}$$

The Nusselt number for convective heat transfer can be calculated directly from Equation (33). To calculate the Nusselt number due to condensation, the mass transfer coefficient is first determined using the mass transfer Stanton number (Equation (34)). The condensation heat transfer coefficient can then be resolved using Equation (31), from which the condensation Nusselt number is found ($Nu \equiv hd_h/k$).

Blowing (thinning and waviness of condensate layer due to flux perpendicular to the flow) can have a significant influence on the total heat transfer. In the model blowing effects are considered by using the blowing parameter, detailed in Ref. [44] (Equation (38)) to modify the Stanton number found using Equation (37). Nusselt numbers are then re-calculated and corrected for entrance effects, shown in Equation (39).

$$St_b = St\frac{b_h}{exp(b_h) - 1} \tag{37}$$

$$b_h = \frac{\dot{m}_{cd}}{\dot{m}_b St} = -\frac{JaNu_{cd}}{StPr_bRe_b}\frac{Nu_f}{Nu_f + (Nu_{cv} + Nu_{cd})\frac{k_b}{k_f}} \tag{38}$$

$$Nu_e = \begin{cases} 1.5\left(\frac{x}{d_h}\right)^{-0.16} Nu & \text{if } \frac{x}{d_h} < 12 \\ Nu & \text{if } \frac{x}{d_h} \geq 12 \end{cases} \tag{39}$$

Heat transfer across the condensate film $q_f = h_f(T_i - T_{wall,h})$ can then be compared to heat transfer across the non-condensable boundary layer $q_b = (h_{cd} + h_{cv})(T_b - T_i)$, iterating the interface temperature (T_i) until the two become equal. In the case of a superheated stream, only the convection heat transfer coefficient is considered.

After the overall heat transfer for a single section has been found, it is possible to determine the exit properties of the hot side flow for that section. Pressure gradient is established from the friction factor, followed by calculating the hot side exit temperature. When the bulk flow temperature is above the dew point and the wall temperature below, an energy balance is performed using Equation (40) [47], where n refers to the condenser section, $\dot{m}_{cd}$ the rate of condensation and q_{gas} is the convective heat transfer between the bulk and condensate interface, calculated from h_{cv} only.

$$T_{b,n+1} = \frac{(\dot{m}_{N_2}C_{p,N_2} + \dot{m}_{O_2}C_{p,O_2} + \dot{m}_{v,n}C_{p,v})T_{b,n} - q_{gas} - \dot{m}_{cd}C_{p,v}T_{i,n}}{\dot{m}_{N_2}C_{p,N_2} + \dot{m}_{O_2}C_{p,O_2} + \dot{m}_{v,n+1}C_{p,v}} \tag{40}$$

Since Equation (40) does not account for the saturation limit of water vapour, when the bulk flow is at saturation a separate energy balance is performed using the enthalpy of the bulk flow at saturation (Equation (41)). The hot side section exit temperature can then be found as a function of the exit enthalpy ($H_{out} = H_{in} - q_t$) and pressure using Equation (41) where $\dot{m}_{v,max}$ is the maximum vapour flow rate at saturation.

$$H_h = f(T,P) = \left(\dot{m}_{N_2}C_{p,N_2} + \dot{m}_{O_2}C_{p,O_2} + \dot{m}_l C_{p,l}\right)(T - T_0) + \dot{m}_{v,max}\left(\Delta H_v + C_{p,v}(T - T_0)\right) \tag{41}$$

Condensing radiator

The hot side section of the condensing radiator model is validated using data from Refs. [47], who instrumented a single radiator tube in annular flow with liquid water and conducted tests across a range of flow rates at different inlet temperatures and vapour mass fractions. Fig. 5a and b compare the experimental heat transfer and condensate rates respectively to those predicted by the model. Overall the model shows a good agreement with the experimental data, with a mean deviation less than 14% across a wide range of saturated and unsaturated operating conditions.

Cold side section heat transfer is calculated in the same way as the air side of the liquid cooled radiator described in the single phase radiator section for air flow over louvred fins. The same radiator geometry, shown in Table 2, is used for both radiators in this study with the exception of the tube depth, which was increased from 2.5 mm to 5 mm for the condensing radiator to prevent excessive pressure drop. Overall heat transfer for each section in the condenser model is determined by comparing the predicted hot and cold side heat transfers, then iterating the wall temperature until the two sides converge.

Compact plate condenser

The compact plate condenser is used in layout C to transfer heat between the cathode exhaust and vehicle coolant loop. Assuming the flow is evenly split between the different plates, heat transfer is determined for a single set of plates (one hot and one cold plate) in a single pass counterflow layout then scaled up across the whole heat exchanger. Heat transfer area is determined as the surface area of the plate multiplied by the surface enlargement factor caused by the chevron surface enhancements. The influence of the surface enhancements on the boundary layer have not been considered in this model.

Cold side Nusselt number is found using the empirical correlation of [46] for single phase flow inside a compact plate heat exchanger using a 22° chevron angle (Equation (42)). Predicted hot and cold side heat transfer are compared and the wall temperature iterated until the two sides converge for each section moving from hot side inlet to exit. Further iteration is then required to determine the cold side temperature profile since the heat exchanger is in a counterflow arrangement. The number of required iterations are reduced by using the cold side temperature profile from the previous time step as an initial estimate.

$$Nu = 0.103Re^{\frac{4}{3}}Pr^{\frac{1}{3}} \tag{42}$$

The compact condenser model was validated using data for a single hot side plate from Refs. [46], across a representative range of flow rates and inlet temperature the mean absolute predicted heat transfer error was 2.4%. Fig. 6 shows the experimental and predicted hot side temperature profiles based on an 80 °C inlet with a Reynolds number of 1600.

Please cite this article in press as: Fly A, Thring RH, A comparison of evaporative and liquid cooling methods for fuel cell vehicles, International Journal of Hydrogen Energy (2016), http://dx.doi.org/10.1016/j.ijhydene.2016.06.089

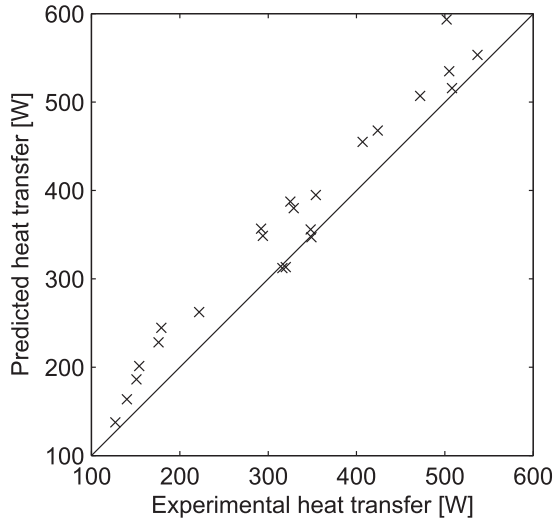

(a) Experimental vs. Predicted heat transfer

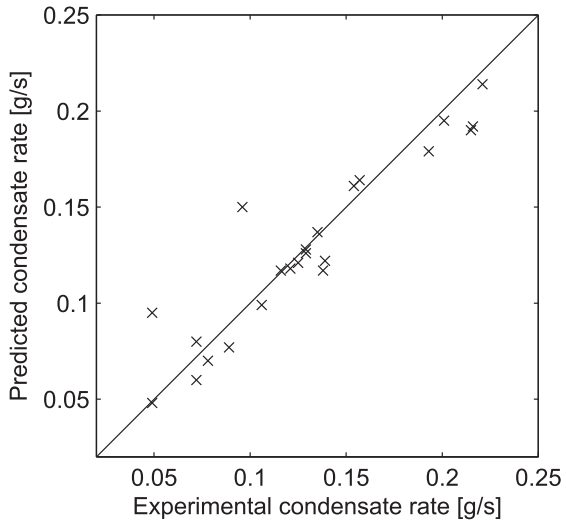

(b) Experimental vs. Predicted condensate rates

Fig. 5 – Condenser tube validation, data from Ref. [47].

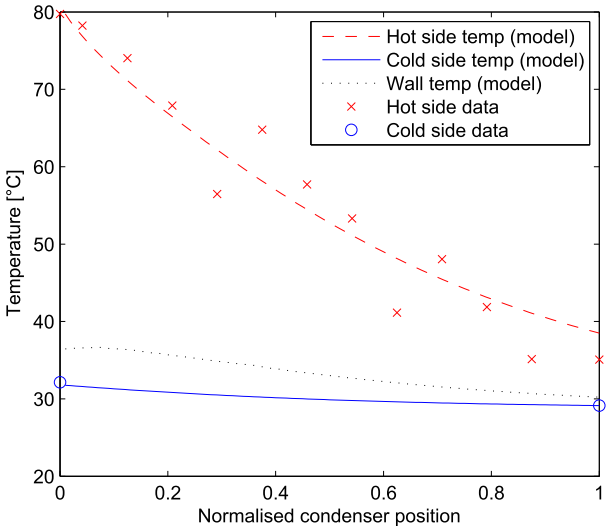

Fig. 6 – Experimental condenser validation [46].

Humidification (liquid cooled only)

To prevent membrane drying in the liquid cooled system, the cathode inlet flow is humidified using vapour transfer from the cathode exhaust. A best case humidifier has been modelled, vapour is transferred either up to the point of requested relative humidity (0–1), or until the molar concentration of water vapour in the exhaust and inlet are equal, whichever is less. The maximum vapour flow rate, at which the molar concentrations are equal, is found using Equation (43).

$$\dot{m}_{v,max} = \dot{m}_{H_2O,c\ \ out}\frac{\dot{m}_{N_2}M_{O_2} + \dot{m}_{O_2,hum,\ \ out}M_{N_2}}{\dot{m}_{N_2}M_{O_2} + \dot{m}_{O_2,ca,\ \ out}M_{N_2}} \tag{43}$$

Once vapour transfer has been determined, an energy balance is performed to calculate the new humidifier exit temperature. The humidity and desired vapour transfer are then re-evaluated at the new humidifier exit temperature, this process is repeated until further iterations yield a change in temperature less than 0.01 °C.

Cooling (liquid cooled only)

Heat is removed from the liquid cooled stack via circular cooling channels in the bi-polar plates between cells. Coolant heat transfer coefficient is determined using the Dittus–Boelter correlation for turbulent pipe flow [41]. Assuming equal cooling flow to each tube, heat transfer is evaluated for a single tube then multiplied by the number of tubes within the entire stack. The ε-*NTU* method is used with an infinite heat capacity ratio due to the uniform cell temperature assumption, effectiveness is found using Equation (44) [41] and heat transfer using Equation (45).

$$\varepsilon = 1 - exp(-NTU) \tag{44}$$

$$\dot{Q}_{coolant} = \varepsilon\dot{m}_{coolant}C_{p,coolant}(T_s - T_{coolant}) \tag{45}$$

Coolant flow rate is regulated through a proportional integral (PI) controller to achieve a target coolant temperature difference across the stack of 5 °C, the minimum flow rate is 10l pm. Stack temperature is regulated by changing the amount of coolant which by-passes the radiator, also using a PI controller, this method has been used with good effect by Hu et al [20] among others.

Coolant tank

The thermal inertia of the coolant tank is modelled using a first order differential energy balance similar to the fuel cell stack. Heat into the cooling loop comes from either the compact plate condenser (Layout C) or the fuel cell stack (Layout A). In both cases thermal energy is removed through the radiator. Equation (46) shows the energy balance for the liquid cooled (Layout A) coolant tank.

Please cite this article in press as: Fly A, Thring RH, A comparison of evaporative and liquid cooling methods for fuel cell vehicles, International Journal of Hydrogen Energy (2016), http://dx.doi.org/10.1016/j.ijhydene.2016.06.089

$$m_{coolant}C_{p,coolant}\frac{dT_{tank}}{dt} = \dot{Q}_{coolant} - \dot{Q}_{rad} \quad (46)$$

Results

The evaporatively cooled fuel cell stack and heat exchanger models used in this study have each been individually validated across realistic operating conditions. It is therefore reasonable to assume that when combined, the models will also give representative results at a system level. Using this method, simulations for all three fuel cell systems were implemented using MATLAB Simulink with base parameters for 'typical' hybrid fuel cell vehicle shown in Table 1.

System temperatures

Steady state stack temperature across different current densities for both the Liquid cooled and evaporatively cooled systems are shown in Fig. 7. Since the liquid cooled stack temperature is regulated by the radiator by-pass position which has some degree of integral control, the steady state error is zero and stack temperature is equal to target temperature of 80 °C. In the evaporatively cooled stack, liquid water is supplied to achieve a desired 100% cathode flow channel relative humidity. As current density increases, the air flow rate to achieve a desired stoichiometry will increase, allowing more water vapour to be evaporated and more heat to be removed from the stack at a rate linearly proportional to current density. Due to irreversible voltage losses, the increase in heat generation with current density is non-linear, resulting in a small increase in stack temperature with current density. However, the exponential nature of the saturation pressure keeps the temperature increase within acceptable limits throughout the ideal (ohmic) current density region of the stack. Between (0.2–1.0 A/cm^2) the increase in stack temperature was 2.4 °C, without the need for thermal management feedback control, provided humidity is maintained. Increasing operating pressure also increases stack operating temperature due to the reduced vapour mass fraction leaving the stack for the same saturation pressure. This may lead to the maximum operating pressure of the system being dictated by the maximum permissible temperature of the membrane.

Transient stack and coolant temperatures over a current profile for both the liquid cooled system (Layout A) and evaporatively cooled system with intermediate condenser (Layout C) are displayed in Fig. 8, ambient temperature is 25 °C, radiator air speed is constant at 6 m/s. Both systems are able to regulate stack temperature to within acceptable limits throughout the drive cycle, ±0.93 °C for the liquid cooled system using PI feedback control of the radiator by-pass and ±1.00 °C for the evaporatively cooled system being self regulating. To reduce thermal gradients within the liquid cooled stack coolant temperature rise across stack is limited to 5 °C, at low loads heat exchanger effectiveness is high and coolant

Table 1 – Fuel cell parameters.

Parameter	Value
Rated power	50 kW
Maximum net efficiency (LHV)	56%
Cells in stack	360
Active area per cell	200 cm^2
Cathode stoichiometry	2.5
Anode stoichiometry	1.03
Mass of stack (m_s)	30 kg
Specific heat of stack (C_{ps})	3.5 kJ/kgK
Stack cathode volume	0.01 m^3
Membrane thickness (z)	100 μm
Internal current density (i_n)	1.5×10^{-4} A/cm^2
Mass transport coefficient (a_{trans})	3×10^{-4}
Mass transport coefficient (b_{trans})	3.0
Exchange current density at STP	3.2×10^{-8} A/cm^2
Molar mass membrane [38] (M_{mem})	1.1 kg/mol
Dry density membrane [49] (ρ_{dry})	1.98 g/cm^3
Cooling tubes per plate	50
Cooling tube diameter	2 mm
Stack cooling heat transfer area	5 m^2
Compressor efficiency	70%

Table 2 – Heat exchanger parameters.

Parameter	Value
Compact plate condenser	
Coolant flow rate	60lpm
Thickness of single plate	1 mm
Surface enlargement factor	1.12
Plate effective hydraulic diameter	4 mm
Total heat transfer area	3 m^2
Radiator [43]	
Coolant tank capacity	10 l
Fin length	8.59 mm
Fin pitch	2.5 mm
Fin thickness	0.1 mm
Louvre height	0.315 mm
Louvre length	6.74 mm
Louvre pitch	1.14 mm
Tube depth	21.58 mm
Tube height (condensing)	5.0 mm
Tube height (liquid)	2.5 mm
Tube thickness	0.32 mm

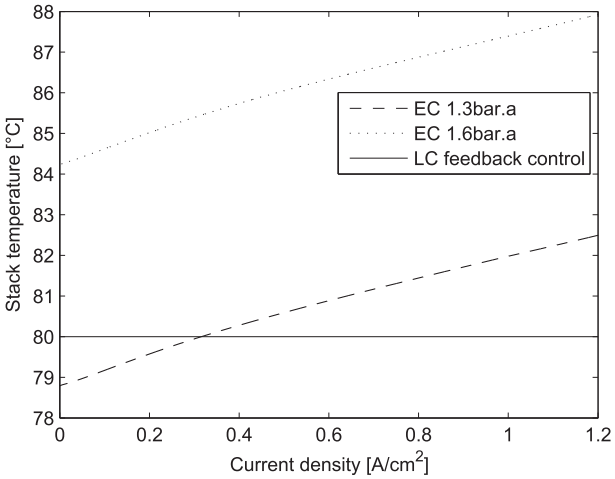

Fig. 7 – Stack temperatures of EC and LC system.

Please cite this article in press as: Fly A, Thring RH, A comparison of evaporative and liquid cooling methods for fuel cell vehicles, International Journal of Hydrogen Energy (2016), http://dx.doi.org/10.1016/j.ijhydene.2016.06.089

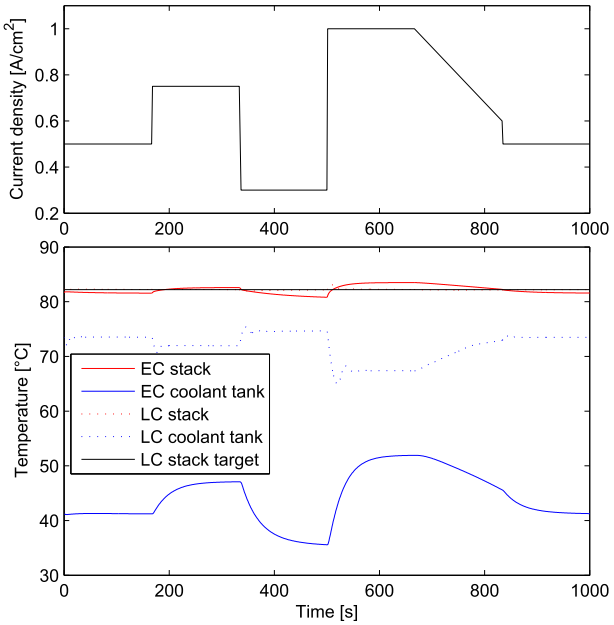

Fig. 8 – Temperatures across transient current profile.

exits close to stack temperature. To maintain the target coolant temperature increase then requires the coolant tank temperature to be close to stack temperature as seen in Fig. 8. In contrast, since the coolant in the evaporatively cooled system does not come into contact with the stack there is no regulation on temperature and during periods of low load the coolant tank temperature tends to ambient temperature. This provides a thermal inertia which can be utilized for increased heat transfer and water collection during short periods of high load operation. A lower coolant temperature is also beneficial for ancillaries cooling, such as the motors and power electronics.

Evaporatively cooled layout

It is possible to compare the performance of the two different evaporatively cooled system layouts by observing the net water flow across different current densities for the same operating conditions and radiator frontal area. Net water flow is calculated as the rate of water consumed in hydrating and cooling the stack ($\dot{m}_{H_2O,inject}$), subtracted from the rate of liquid water extracted from the cathode exhaust stream after the condenser (Equation (47)).

$$\dot{m}_{H_2O,net} = \dot{m}_{H_2O,collect} - \dot{m}_{H_2O,inject} \quad (47)$$

Fig. 9 demonstrates net water flow of both layouts across a steady state polarisation, along with the maximum possible net water flow (reaction product water). Simulations were conducted with an ambient temperature of 25 °C and a radiator air velocity of 4 m/s. The condensing radiator layout is shown to perform better than the intermediate condenser across all loads. The point at which the system enters net water loss is 1.40 A/cm^2 for the condensing radiator system (layout B) and 0.89 A/cm^2 for the intermediate condenser system (layout C). The maximum net flow of layout B is 2.98 g/s at 0.78 A/cm^2 current density compared to 1.92 g/s at 0.49 A/cm^2 for layout C. The improvement of layout B compared to layout C is primarily because of higher hot side heat transfer coefficients within the radiator due to condensation which are not seen in the liquid cooled radiator used in layout C. Fig. 10 compares the hot side heat transfer coefficient profile of the condensing radiator to the liquid cooled radiator, the only differences between the two radiators are the hot side working fluids and tube diameter. At low to mid current densities the hot side of the condensing radiator is cooled close to the tube inlet, causing the mass fraction of non-condensable gas to drop, reducing the heat transfer coefficient below that of the liquid cooled radiator. At higher current densities, increased air flow and a slight elevation in temperature lead to both a higher Reynolds number and lower mass fraction of non-condensable, increasing heat transfer coefficient. As current density increases, so does the gap between net water flow of the two systems, which can be seen in Fig. 9.

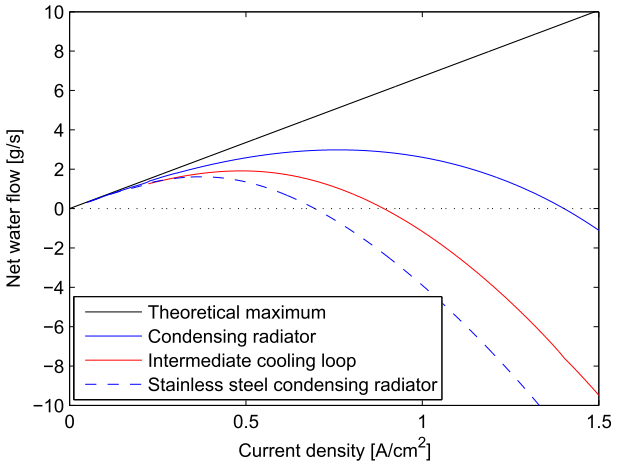

Fig. 9 – EC system net water flow for different layouts.

For the collected water to remain de-ionised conventional aluminium heat exchangers are not suitable [1]. In the condensing radiator layout (Layout B) condensate comes into direct contact with the radiator tubes. To avoid contamination either the tube internals need to be coated or a different material used for the radiator. The dashed line in Fig. 9 shows the

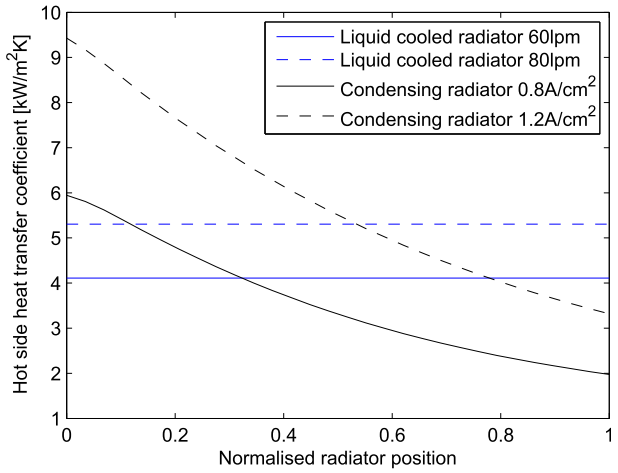

Fig. 10 – Comparison of Radiator hot side heat transfer coefficients.

Please cite this article in press as: Fly A, Thring RH, A comparison of evaporative and liquid cooling methods for fuel cell vehicles, International Journal of Hydrogen Energy (2016), http://dx.doi.org/10.1016/j.ijhydene.2016.06.089

net water flow if the aluminium radiator were replaced with stainless steel of the same geometry, the reduction in performance is due to the lower thermal conductivity of stainless steel. Whilst the performance of the stainless steel radiator could potentially be improved through geometry optimisation, this demonstrates the requirement for heat exchangers specifically designed for use with evaporatively cooled fuel cell vehicles.

Heat exchange area

The radiator frontal areas required for water and thermal balance of all three system layouts at different ambient temperatures for 1.25 A/cm^2 constant current density (55 kW net electrical power) with a radiator air velocity of 5 m/s are shown in Fig. 11. The radiator core size for the liquid cooled system has been calculated to give a steady state stack temperature equal to the evaporatively cooled system, the by-pass valve is fully opened and at maximum coolant flow rate (60lpm). Radiator fin and tube geometry (Table 2) is the same for all three layouts excluding the tube depth which is 2.5 mm for the liquid cooled radiator and 5 mm for the condensing radiator to reduce pressure drop. For all the ambient temperatures considered layout B (Evaporatively cooled, condensing radiator) needed the minimum radiator heat exchange area to maintain thermal and water balance, the worst performing design was layout C (Evaporatively cooled, intermediate cooling loop) which needed a considerably higher heat exchange area, especially at high ambient temperatures. The better performance of the condensing radiator layout is primarily caused by the presence of phase change within the radiator tubes giving rise to higher heat transfer coefficients. The conventional liquid cooled design performed better than layout C because the intermediate cooling loop had a lower temperature at the radiator hot side inlet, reducing the overall temperature difference between coolant and ambient. At an ambient temperature of 35 °C the heat exchange area for layout B is 26.7% less than layout A (liquid cooled) and 62.56% less than layout C (intermediate cooling loop).

For low ambient temperatures the liquid cooled system thermal performance reduces and further reductions in frontal area are not observed. This occurs because the humidification system is unable to transfer enough vapour to the low temperature inlet stream to sufficiently humidify the stack, drying the membrane. Inlet humidity could potentially be increased by increasing the operating pressure, both reducing the required water vapour mole fraction and increasing the compressor exit temperature.

Collection efficiency

In the previous examples it has been assumed that all liquid water present at the exit of the condenser can be collected from the exhaust stream. In reality, liquid separation efficiencies for a well designed cyclone are in the region of 95–99% [48]. Reductions in collection efficiency cause non-linear increases in temperature reduction required to maintain water balance, due to the non-linear saturation pressure of water vapour. Fig. 12 shows how collection efficiency influences required radiator frontal area for layout B, model inputs were 35 °C ambient temperature, 1.0 A/cm^2 current density and 7 m/s radiator air velocity. This is compared to the frontal area requirements for a liquid cooled system operating under identical conditions to achieve the same stack temperature as the 1.3 bar.a evaporatively cooled simulation. The comparison shows that at low operating pressures a high collection efficiency is required to make evaporative cooling better than liquid cooling in terms of radiator requirements (91.0% at 1.3 bar.a). Increasing the operating pressure reduces the required efficiency to make evaporative cooling beneficial (86.5% at 1.7 bar.a), this demonstrates that with current separation efficiencies it is possible to reduce radiator frontal area using evaporative cooling.

Conclusions

A comparison of three different cooling methods for fuel cell vehicles has been presented and it has been shown that radiator frontal area can be reduced up to 27% by changing from liquid to evaporative cooling, provided an aluminium

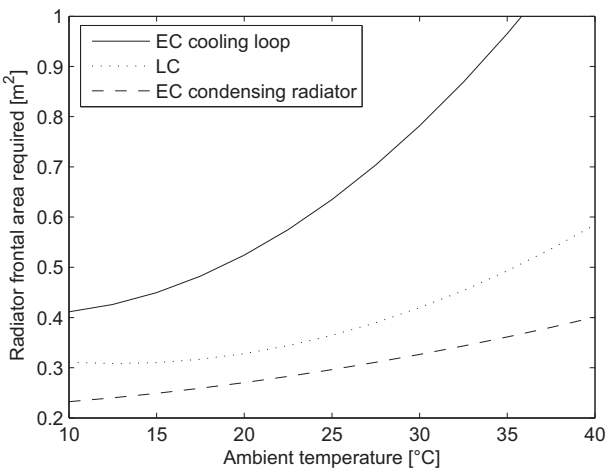

Fig. 11 – Radiator size required for different layouts and ambient temperatures at 1.25 A/cm^2 5 m/s velocity.

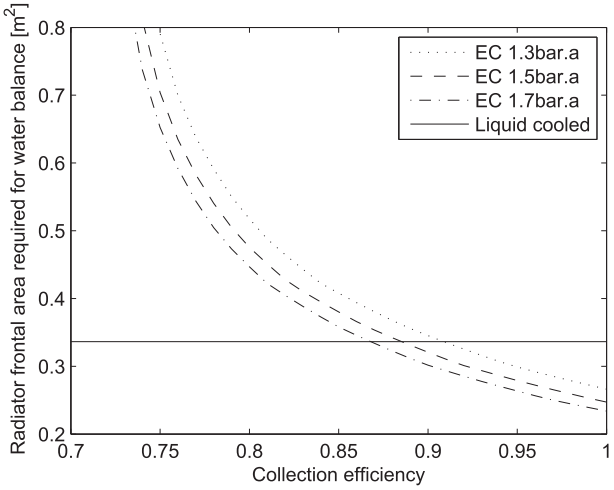

Fig. 12 – Influence of collection efficiency on required radiator frontal area.

Please cite this article in press as: Fly A, Thring RH, A comparison of evaporative and liquid cooling methods for fuel cell vehicles, International Journal of Hydrogen Energy (2016), http://dx.doi.org/10.1016/j.ijhydene.2016.06.089

condensing radiator is used. The primary reason for the improvement seen by the evaporative cooling design is due to phase change within the radiator tubes, although for these benefits to be achieved a high liquid water separation efficiency is required. Contamination issues with aluminium heat exchangers along with a change in working fluid from liquid to two-phase would require conventional radiators to be redesigned, however further improvements may be obtained from optimising the air side geometry to account for the higher heat transfer coefficients of the two phase hot side flow.

Acknowledgements

This work has been funded by the Engineering and Physical Sciences Research Council (EPSRC) under grant number EP/G037116/1.

REFERENCES

[1] Fronk MH, Wetter DL, Masten DA, Bosco A. Pem fuel cell system solutions for transportation. SAE Tech Pap 2000. 2000–01–0373, 2011-32-0644.
[2] Adams JA, Chul Yang W, Oglesby KA, Osborne KD. The development of ford's p2000 fuel cell vehicle. SAE Tech Pap 2000. 2000–01–1061, 2011-32-0644.
[3] Rogg S, Höglinger M, Zwittig E, Pfender C, Kaiser W, Heckenberger T. Cooling modules for vehicles with a fuel cell drive. Fuel Cells 2003;3:153–8.
[4] Zhang G, Kandlikar SG. A critical review of cooling techniques in proton exchange membrane fuel cell stacks. Int J Hydrogen Energy 2012;37:2412–29.
[5] Ryan D, Shang J, Quillivic C, Porter B. Performance and energy efficiency testing of a lightweight fcev hybrid vehicle. Eur Electr Veh Congr (EEVC) 2014.
[6] Ikeya K, Hirota K, Takada Y, Eguchi T, Mizutani K, Ohta T. Development and evaluation of air-cooled fuel cell scooter. JSAE 2011. 2011–32–0644.
[7] Larminie J, Dicks A. Fuel cell systems explained. 2nd ed. Wiley; 2006.
[8] Odabaee M, Mancin S, Hooman K. Metal foam heat exchangers for thermal management of fuel cell systems, an experimental study. Exp Therm Fluid Sci 2013;51:214–9.
[9] Boyd B, Hooman K. Air-cooled micro-porous heat exchangers for thermal management of fuel cells. Int Commun Heat Mass Transf 2012;39(3):363–7.
[10] Afshari E, Ziaei-Rad M, Shariati Z. A study on using metal foam as coolant fluid distributor in the polymer electrolyte membrane fuel cell. Int J Hydrogen Energy 2016;41(3):1902–12.
[11] Chen FC, Gao Z, Loutfy RO, Hecht M. Analysis of optimal heat transfer in a pem fuel cell cooling plate. Fuel Cells 2003;3:181–8.
[12] Baek SM, Yu SH, Nam JH, Kim C-J. A numerical study on uniform cooling of large-scale pemfcs with different coolant flow field designs. Appl Therm Eng 2011;31(8¢9):1427–34.
[13] Sasmito AP, Kurnia JC, Mujumdar AS. Numerical evaluation of various gas and coolant channel designs for high performance liquid-cooled proton exchange membrane fuel cell stacks. Energy 2012;44:278–91.
[14] Kang S, Min K, Mueller F, Brouwer J. Configuration effects of air, fuel, and coolant inlets on the performance of a proton exchange membrane fuel cell for automotive applications. Int J Hydrogen Energy 2009;34:6749–64.
[15] Barbir F. PEM fuel cells. 2nd ed. US: Academic Press; 2013.
[16] Yu S, Jung D. Thermal management strategy for a proton exchange membrane fuel cell system with a large active cell area. Renew Energy 2008;33:2540–8.
[17] Cheng S, Fang C, Xu L, Li J, Ouyang M. Model-based temperature regulation of a pem fuel cell system on a city bus. Int J Hydrogen Energy 2015;40(39):13566–75.
[18] Y. Saygili, I. Eroglu, S. Kincal, Model based temperature controller development for water cooled pem fuel cell systems, Int J Hydrogen Energy 40 615–622.
[19] Yu S, Jung D. A study of operation strategy of cooling module with dynamic fuel cell system model for transportation application. Renew Energy 2010;35:2525–32.
[20] Hu P, Cao G-Y, Zhu X-J, Hu M. Coolant circuit modeling and temperature fuzzy control of proton exchange membrane fuel cells. Int J Hydrogen Energy 2010;35:9110–23.
[21] Ahn J-W, Choe S-Y. Coolant controls of a pem fuel cell system. J Power Sources 2008;179:252–64.
[22] Islam MR, Shabani B, Rosengarten G, Andrews J. The potential of using nanofluids in pem fuel cell cooling systems: a review. Renew Sustain Energy Rev 2015;48:523–39.
[23] Zakaria I, Azmi WH, Mamat AMI, Mamat R, Saidur R, Talib SFA, et al. Thermal analysis of al_2 o_3 water ethylene glycol mixture nanofluid for single pem fuel cell cooling plate: an experimental study. Int J Hydrogen Energy 2016;41(9):5096–112.
[24] Silva AP, Galante RM, Pelizza PR, Bazzo E. A combined capillary cooling system for fuel cells. Appl Therm Eng 2012;41:104–10.
[25] Garrity PT, Klausner JF, Mei R. A flow boiling microchannel evaporator plate for fuel cell thermal management. Heat Transf Eng 2007;28:877–84.
[26] Soupremanien U, LePerson S, Favre-Marinet M, Bultel Y. Tools for designing the cooling system of a proton exchange membrane fuel cell. Appl Therm Eng 2012;40:161–73.
[27] Meyers JP, Darling RM, Evans C, Balliet R, Perry ML. Evaporatively-cooled pem fuel-cell stack and system. In: Proton exchange membrane fuel cells 6–210th electrochemical society meeting. Electrochemical Society Inc; 2006. p. 1207–14.
[28] Wood DL, Yi JS, Nguyen TV. Effect of direct liquid water injection and interdigitated flow field on the performance of proton exchange membrane fuel cells. Electrochimica Acta 1998;43(24):3795–809.
[29] Warburton A, Mossop D, Burslem B, Rama P, Adcock P, Cole J, et al. Development of an evaporatively cooled hydrogen fuel cell system and its vehicle application. SAE Tech Pap 2013. 2013–01–0475, 2011-32-0644.
[30] Hwang SH, Kim MS. An experimental study on the cathode humidification and evaporative cooling of polymer electrolyte membrane fuel cells using direct water injection method at high current densities. Appl Therm Eng. 2016;99:635–44.
[31] Schultze M, Horn J. A control oriented simulation model of an evaporation cooled polymer electrolyte membrane fuel cell system. In: 18th International Federation of Automatic Control World Congress, Milan, Italy; 2011. p. 14790–5.
[32] Fly A, Thring RH. Temperature regulation in an evaporatively cooled proton exchange membrane fuel cell stack. Int J Hydrogen Energy 2015;40(35):11976–82.

Please cite this article in press as: Fly A, Thring RH, A comparison of evaporative and liquid cooling methods for fuel cell vehicles, International Journal of Hydrogen Energy (2016), http://dx.doi.org/10.1016/j.ijhydene.2016.06.089

[33] A. Fly, reportThermal and water management of evaporatively cooled fuel cell vehicles, PhD thesis, Loughborough University.
[34] Fly A, Thring RH. Model based investigation of liquid water injection strategies for evaporatively cooled pem fuel cells. In: ASME 2015 13th International Conference on Fuel Cell Science, Engineering and Technology; 2015. FUELCELL 2015–49196.
[35] Sulek M, Adams J, Kaberline S, Ricketts M, Waldecker JR. In situ metal ion contamination and the effects on proton exchange membrane fuel cell performance. J Power Sources 2011;196:8967–72.
[36] Springer TE, Zawodzinski TA, Gottesfeld S. Polymer electrolyte fuel cell model. J Electrochem Soc 1991;138:2334–42.
[37] Dutta S, Shimpalee S, Zee JWV. Numerical prediction of mass-exchange between cathode and anode channels in a pem fuel cell. Int J Heat Mass Transf 2001;44:2029–42.
[38] Chen Y-S, Peng H. A segmented model for studying water transport in a pemfc. J Power Sources 2008;185:1179–92.
[39] Pukrushpan JT, Peng H, Stefanopoulou AG. Control-oriented modeling and analysis for automotive fuel cell systems. J Dyn Syst Meas Control 2004;126:14–25.
[40] Rabbani A, Rokni M. Effect of nitrogen crossover on purging strategy in pem fuel cell systems. Appl Energy 2013;111:1061–70.
[41] Incropera FP, Dewitt DP. Introduction to heat transfer. 4th ed. John Wiley and Sons; 2002.
[42] Chang Y-J, Wang C-C. A generalized heat transfer correlation for iouver fin geometry. Int J Heat Mass Transf 1997;40:533–44.
[43] Jung D, Assanis DN. Numerical modeling of cross flow compact heat exchanger with louvered fins using thermal resistance concept. SAE tech pap 2006. 2006–01–0726.
[44] No HC, Park HS. Non-iterative condensation modeling for steam condensation with non-condensable gas in a vertical tube. Int J Heat Mass Transf 2002;45:845–54.
[45] Colburn AP, Hougen OA. Design of cooler condensers for mixtures of vapors with noncondensing gases. Ind Eng Chem 1934;26:1178–82.
[46] Fly A, Thring R. Condensation of water from saturated air in a compact plate condenser with application to water balance in proton exchange membrane fuel cell systems. In: 15th International Heat Transfer Conference; 2014. pp. IHTC–8969.
[47] S. Krishnaswamy, reportFilmwise condensation inside a non-circular tube in the presence of forced convection and a non-condensing gas, PhD thesis: Queen Mary University of London.
[48] Kurokawa J, Ohtaki T. Gas-liquid flow characteristics and gas-separation efficiency in a cyclone separator. ASME Gas Liq Flows 1995;225:51–7.
[49] Pasaogullari U, Wang CY. Liquid water transport in gas diffusion layer of polymer electrolyte fuel cells. J Electrochem Soc 2004;151:A399–406.

Nomenclature

A: Area, m^2
b_h: Blowing parameter
C: Heat capacity, J/K
C_n: Nozzle discharge coefficient
C_p: Specific heat, J/kgK
D_λ: Membrane diffusivity, cm^2/s
d_h: Hydraulic diameter, m
E_c: Cathode activation energy, kJ/mol
E_n: Reversible cell voltage, V
F: Faraday constant, C/mol
f: Friction factor
g: Mass transfer coefficient, kg/m^2 s
H: Enthalpy, J/kg
h: Heat transfer coefficient, W/m^2 K
i: Current density, A/cm^2
Ja: Jakob number
j: Colburn factor
k: Thermal conductivity, W/mK
L: Length, m
M: Molar mass, kg/mol
m: Mass, kg
NTU: Number of transfer units
Nu: Nusselt number
P: Pressure, Pa
Pr: Prandtl number
$\dot{Q}$: Energy, W
q: Heat transfer, W/m^2
Re: Reynolds number
Sc: Schmidt number
St: Stanton number
T: Temperature, K
t: Time/Wall thickness, s, m
U: Overall heat transfer coefficient, W/m^2 K
V: Voltage/Velocity, V, m/s
W: Mass fraction
x: Distance from channel inlet, m
z: Membrane thickness, m

Subscript

0: Value at STP
an: Anode
b: Bulk flow
c: Cold side
ca: Cathode
cd: Condensation
cv: Convection
e: Entrance
f: Condensate film
h: Hot side
hum: Humidifier
ht: Heat transfer
i: Condensate layer interface
l: Liquid water
mt: Mass transfer
s: Fuel cell stack
t: Total
v: Water vapour
w: Wall

Greek

α: Charge transfer coefficient
γ: Pressure dependency coefficient (0.5)
ΔH_v: Enthalpy of vapourisation, J/kg
$\Delta\hat{h}$: Enthalpy change, J/molK
$\Delta\hat{s}$: Entropy change, J/mol
δ: Condensate layer thickness, m
ε: Heat exchanger effectiveness
η: Radiator fin efficiency
λ: Membrane water content
ρ: Density, kg/m^3
τ: Water entrainment constant
Ω: Membrane resistance, Ω/cm^2
ω: Surface roughness, m

Please cite this article in press as: Fly A, Thring RH, A comparison of evaporative and liquid cooling methods for fuel cell vehicles, International Journal of Hydrogen Energy (2016), http://dx.doi.org/10.1016/j.ijhydene.2016.06.089